

Optically Detected Magnetic Resonance for Selective Imaging of Diamond Nanoparticles

Margaret E. Robinson,[†] James D. Ng,[†] Huilong Zhang,[§] Joseph T. Buchman,^{||} Olga A. Shenderova,[‡] Christy L. Haynes,^{||} Zhenqiang Ma,[§] Randall H. Goldsmith,[†] and Robert J. Hamers^{*,†}

[†]Department of Chemistry, University of Wisconsin—Madison, 1101 University Avenue, Madison, Wisconsin 53706, United States

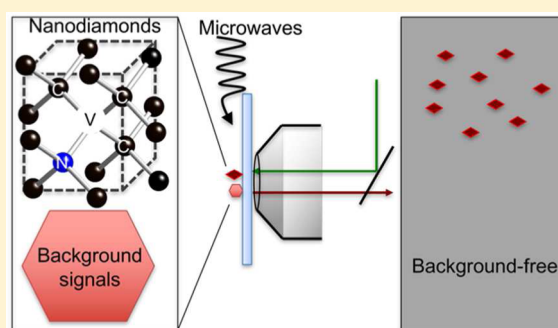
[‡]Adamas Nanotechnologies, 8100 Brownleigh Drive, Raleigh, North Carolina 27617, United States

[§]Department of Electrical and Computer Engineering, University of Wisconsin—Madison, 3445 Engineering Hall, 1415 Engineering Drive, Madison, Wisconsin 53706, United States

^{||}Department of Chemistry, University of Minnesota, 207 Pleasant Street SE, Minneapolis, Minnesota 55455, United States

S Supporting Information

ABSTRACT: While there is great interest in understanding the fate and transport of nanomaterials in the environment and in biological systems, the detection of nanomaterials in complex matrices by fluorescence methods is complicated by photodegradation, blinking, and the presence of natural organic material and other fluorescent background signals that hamper detection of fluorescent nanomaterials of interest. Optically detected magnetic resonance (ODMR) of nitrogen–vacancy (N_V) centers in diamond nanoparticles provides a pathway toward background-free fluorescence measurements, as the application of a resonant microwave field can selectively modulate the intensity from N_V centers in nanodiamonds of various diameters in complex materials systems using on-resonance and off-resonance microwave fields. This work represents the first investigation showing how nanoparticle diameter impacts the N_V center lifetime and thereby directly impacts the accessible contrast and signal-to-noise ratio when using ODMR to achieve background-free imaging of N_V^- nanodiamonds in the presence of interfering fluorophores. These results provide new insights that will guide the choice of optimum nanoparticle size and methodology for background-free imaging and sensing applications, while also providing a model system to explore the fate and transport of nanomaterials in the environment.



One of the key challenges of analytical chemistry is to selectively identify individual species within complex systems. An emerging problem of particular significance and difficulty is to understand the fate and transport of nanomaterials in environmental and biological systems.^{1–6} While the past decade has witnessed outstanding progress in the development of single-photon and subdiffraction optical methods,^{7–9} the use of fluorescence methods to characterize nanomaterials is hampered by the fact that most fluorescent nanoparticles are unstable over the extended time course (frequently days to weeks) associated with biological exposure studies,^{10–13} and complex background signals associated with environmental matrices frequently interfere with emission from nanoparticles of interest.^{14,15} Organic chromophores can be grafted onto nanoparticle surfaces but can be chemically ligated by enzymes and other molecules, are subject to bleaching under intense illumination, and can exhibit cytotoxicity.¹⁶ Consequently, there remains an unmet need for highly stable and selective fluorescent nanoparticles that are nontoxic and will not degrade over extended times in environmental and/or biological media, even under intense illumination.^{17,18} A particularly acute challenge in environmental systems is to

distinguish fluorescence of the fluorophore probe from competing optical signals such as scattering and autofluorescence.¹⁹

Diamond nanoparticles containing N_V centers have recently emerged as a nanomaterial of great potential interest for biological and environmental imaging.^{20–22} N_V centers consist of a substitutional N atom with an adjacent vacancy, forming a highly stable, nonbleachable solid-state fluorophore that exists in neutral (N_V^0) and negative (N_V^-) charge states. N_V^- centers can be excited using easily accessible visible wavelengths and emit at wavelengths of 638–800 nm, a region well-suited to imaging in biological samples.^{23,24} Furthermore, the high chemical stability and ability to covalently functionalize the surface of diamond provides a pathway to tailor the surface properties of N_V^- nanodiamonds in a flexible and highly stable manner.^{25–27} The negatively charged N_V center, N_V^- , is a particularly novel fluorophore because its fluorescence intensity is sensitive to the presence of magnetic fields²⁸ and can be

Received: August 6, 2017

Accepted: November 13, 2017

Published: November 13, 2017

modulated by resonant excitation with a weak microwave excitation,²⁹ a technique known as optically detected magnetic resonance (ODMR).³⁰ ODMR is enabled by the fact that the N_V^- defect is a triplet spin system with magnetic sublevels separated by microwave frequencies and by relaxation dynamics that make the intensity of N_V^- fluorescence sensitive to the distribution of spins into these sublevels. ODMR is important for imaging applications because it provides a way to selectively modulate the intensity of N_V^- -containing nanodiamonds using relatively weak microwave fields, while the vast majority of other fluorescent moieties remain unaffected by the microwaves. Thus, ODMR provides a way to selectively identify fluorescence from diamond nanoparticles in the presence of autofluorescence, scattering, and other spectrally overlapped background signals.^{28,31} In addition to imaging in biological systems,^{29,32,33} ODMR can also be used in principle as a probe of local magnetic fields,^{34–38} electric fields,³⁹ spin,⁴⁰ and temperature.⁴¹ Thus, ODMR in nanodiamond has great potential as a quantum-based analytical tool for addressing a wide range of analytical sensing and selective imaging problems.

Although the properties of N_V centers have been widely studied in bulk diamond,⁴² the factors controlling the use of ODMR to achieve selective imaging of nanodiamonds in the presence of background emitters remain poorly understood.^{43–47} Of particular importance is that while the charge state and dynamics of N_V centers have been known to depend on nanoparticle size,^{48–52} the manner in which nanoparticle size influences the underlying dynamics and the resulting contrast and signal-to-noise ratio of ODMR for selective imaging in environmental and biological systems has not been established previously.

Here, we present studies of the critical factors controlling the ability to selectively image N_V^- nanodiamond in the presence of other fluorescent moieties using ODMR in a full-frame imaging configuration and in spectroscopic mode, using N_V^- -containing nanodiamonds of different sizes derived from the same starting material and thereby having a constant density of N_V^- centers. We demonstrate selective imaging of N_V^- nanodiamonds down to 40 nm diameter by direct digital subtraction of full-frame images acquired with a weak microwave field alternatively applied off-resonance and on-resonance. Full-frame imaging and spectroscopically resolved data using nanodiamonds of different sizes derived from a common starting material (thereby ensuring constant N_V concentration) show that the selectivity associated with ODMR imaging decreases for small nanodiamonds due to both a shift in the N_V charge state from the negatively charged N_V^- center to the neutral N_V^0 center and due to nonradiative relaxation processes associated with the nanodiamond surfaces. Our results highlight the important physical processes and imaging conditions that control the signal-to-noise ratio associated with the use of ODMR to achieve selective imaging of nanodiamond in the presence of background signals such as nondiamond fluorescence and/or scattering. These insights will inform the use of N_V^- -containing nanodiamonds in background-free imaging and guide the understanding of how to use the unique magnetic resonance properties of N_V nanodiamond to enable new approaches to background-free, selective imaging of nanomaterials in complex matrices.

EXPERIMENTAL SECTION

Nanoparticles. Suspensions of oxidized, size-selected (0.1% by weight) nanodiamond with enhanced concentrations of N_V^-

centers were provided by Adámas Nanotechnologies (Raleigh, NC, USA) with nominal diameters ranging from 10 to 100 nm. A 15 μm diameter N_V^- -implanted diamond powder was also provided. N_V^- centers were produced by irradiating 15 μm and 100 nm particles with 2 MeV electrons to a dose of $5 \times 10^{18} \text{ e}^-/\text{cm}^2$, followed by annealing at 850 °C for 2 h and cooling to room temperature. Nanoparticles with 10, 20, 30, 40, and 60 nm diameters were made by mechanically fracturing the larger 15 μm diameter material after activation and annealing. The micrometer-sized particles were milled in a planetary mill using ceramic 1 cm diameter balls, purified from milling media in HF and HNO_3 acids, washed with deionized water, and fractionated into smaller sizes in deionized water media using an ultracentrifuge with up to 45,000 RCF for 4 h for the smallest 10 nm particles. Since N_V^- centers were formed in the 15 μm diamond before fracturing into smaller sizes, our procedure ensures that nanoparticles of all sizes have the same total concentration of N_V^- centers, distributed between the two charge states N_V^0 and N_V^- . The 100 nm particles were processed separately by the same method. The total substitutional nitrogen content (N_s) in 15 μm and 100 nm starting material was determined to be ~ 100 – 120 ppm as measured by electron paramagnetic resonance (EPR).⁵³ The concentration of negatively charged N_V^- centers was also determined by EPR for each size, yielding values of 4 ppm for 15 μm , 2.5 ppm for 100 nm, 1.5 ppm for 60 nm, and below 1 ppm for 10, 20, 30, and 40 nm diameter particles. Detailed procedures for the EPR measurements are in the [Supporting Information \(SI\)](#). Each nanodiamond sample was characterized by dynamic light scattering (Malvern Zetasizer Nano ZS) and by transmission electron microscopy (TEM) to assess particle size and distribution (see the [SI](#)).

Measurement of Emission Spectra. Spectra were measured using the apparatus depicted in [Figure 1](#). Emission

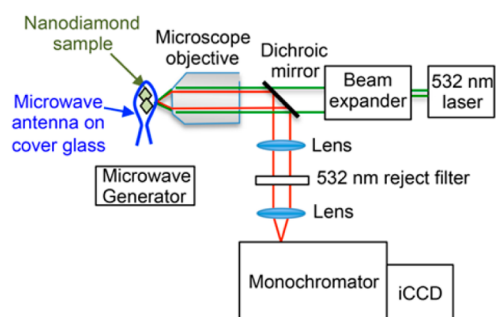


Figure 1. Optical apparatus for performing emission spectra, imaging, and optically detected magnetic resonance experiments.

spectra were collected using a 532 nm continuous-wave diode pumped solid-state laser (Opto Engine LLC, MLL-FN-532-500m) typically using 100 mW focused onto the sample using a 40 \times microscope objective. The fluorescence was collected using the same lens, filtered using a dichroic mirror (Semrock, FF533-SDi01-25 \times 36) and a 532 nm line-reject filter (Semrock, NF01-532U-25) and focused into the 25 μm slit of an Andor Shamrock 193i monochromator with a grating blazed at 760 nm and 150 lines/mm. The detector was an Andor iStar intensified CCD (DH334T-18F-03). All spectra presented here were calibrated using the 532 nm laser line. For optical measurements, a small aliquot of 10 μL of nanodiamond solution was dried onto a cover glass. A consistent procedure was followed for deposition of the nanodiamonds using

dispersions of the same mass concentration; consequently, the mass density of nanoparticles and the area density of N_V^- centers are expected to be similar between different samples.

Microwave Modulation. A 50 Ω impedance-matched antenna was fabricated on top of the cover glass using photolithography and metal lift-off processes. This antenna, described previously,⁵⁴ consists of a circular loop approximately 1 mm in diameter. Microwaves were generated by an Agilent E8251A PSG-A series microwave source and amplified by a power amplifier (ZVE-3W-83+ from Minicircuits) with a power gain of 35 dB and a saturated power of 35 dBm. Experiments reported here used 16 dBm output power from the source, before amplification.

Differential Imaging with Microwave Modulation. Differential imaging was performed using the apparatus shown in Figure 1a with a 20 \times microscope objective. Images of the same location were collected using 2.87 GHz (on-resonance) and 2.93 GHz (off-resonance) microwave frequencies. Images were registered and digitally subtracted (off-resonance–on-resonance) to yield a differential image where the fluorescence intensity of the N_V^- centers have been modulated by the resonant microwave field.

Fluorescence Lifetime Measurements. Fluorescence lifetime measurements were collected using a 3 ns, 20 Hz repetition rate 532 nm Nd:YAG-laser (Ekspla, NT 342B-SH-20-AW) to excite nanodiamonds dried onto a CaF₂ disc using a 5 \times microscope objective; the fluorescence was collected using the same lens, filtered using a dichroic mirror (Semrock, FF553-SDi01-25 \times 36) and a 532 nm line-reject filter (Semrock, NF01-532U-25). Fluorescence was collected using a biased Si photodiode (Thorlabs, DET025A) and recorded on an oscilloscope (Agilent Technologies, DSO9404A, 4 GHz). The resulting fluorescence time traces were fit to a single-exponential decay.

RESULTS

Emission and Optically Detected Magnetic Resonance from Nanodiamond Samples. Figure 2a shows typical emission spectra obtained from nanodiamond samples of different diameters. The negatively charged N_V^- center emits with a zero phonon line at 637 nm and a broad phonon sideband extending to nearly 750 nm; the neutral N_V^0 charge state has a zero phonon line at 575 nm and a sideband to longer wavelengths that overlaps with emission from the N_V^- state. These spectra are similar to those reported previously, exhibiting increased emission from the neutral N_V^0 center as nanodiamond size decreases.⁴⁷ The spectra reported here were individually normalized to demonstrate the changes in spectral distribution. The smaller nanodiamonds also show weaker emission overall. At the smallest sizes the emission spectrum exhibits additional features near 550–570 nm arising from Raman scattering from diamond and nondiamond carbon. These features appear more apparent for small-sized nanodiamond because the N_V^- emission is weaker.

Based on the spectra in Figure 2a, we selected nanodiamonds for further investigation by ODMR.³⁰ Figure 2b depicts the overall scheme of resonant-microwave-induced ODMR. ODMR involves three phenomena: (1) optical spin-pumping preferentially pumps spins into a specific magnetic sublevel ($m_s = 0$) of the ground electronic state; (2) the intensity of emitted fluorescence depends on the distribution of spins, with $|e, m_s = 0\rangle \rightarrow |g, m_s = 0\rangle$ transitions more intense than $|e, m_s = \pm 1\rangle \rightarrow |g, m_s = \pm 1\rangle$ transitions; and (3) excitation with microwaves at the

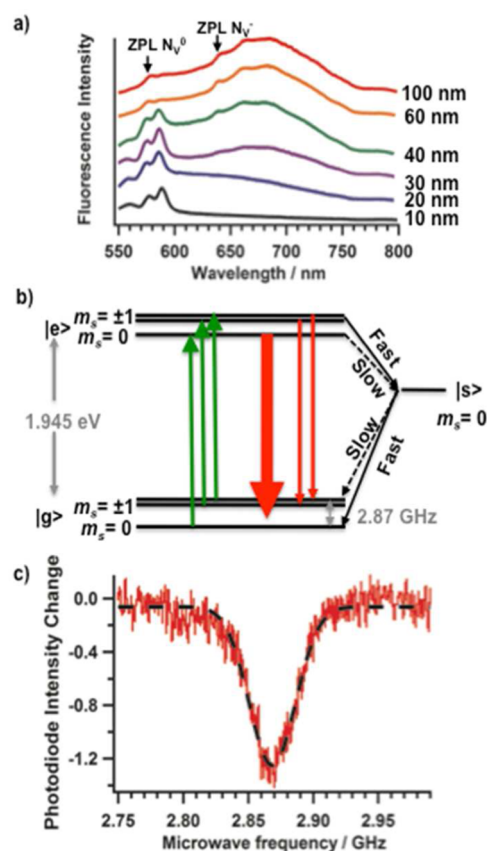


Figure 2. (a) Nanodiamond size-dependent emission of N_V centers with zero phonon lines (ZPLs) of the neutral and negative charge states. (b) Schematic illustration of ODMR, where $|g\rangle$ is the electronic ground state, $|e\rangle$ is the electronic excited state, and $|s\rangle$ is a metastable singlet state. The $|g\rangle$ to $|e\rangle$ transition has a zero phonon line at 637 nm. (c) Microwave frequency-dependent photoluminescence emission on 100 nm nanodiamond. The decrease in emission intensity at 2.87 GHz corresponds to resonant excitation of the spins.

resonance frequency re-distributes the spin population among the magnetic sublevels, thereby altering the intensity of fluorescence.

In ODMR, a continuous-wave excitation at 532 nm excites spins from the ground electronic state $|g\rangle$ ($=^3A_2$) to the first excited electronic state $|e\rangle$ ($=^3E$). Prior studies have shown that the optical transition dipoles are identical for all three magnetic sublevels.⁵⁵ However, intersystem crossing to a dark singlet state occurs faster for the $|e, m_s = \pm 1\rangle$ states than for the $|e, m_s = 0\rangle$ sublevel. Consequently, the intensity of emission from the $|e, m_s = 0\rangle$ sublevel is greater than that from the $|e, m_s = \pm 1\rangle$ sublevels. At sufficiently high excitation intensity, repeated excitation–relaxation cycles lead to depletion of the $|g, m_s = \pm 1\rangle$ sublevels and pumps spins into the $|g, m_s = 0\rangle$ sublevel. The N_V^- center has a zero-field splitting between the $|g, m_s = 0\rangle$ to $|g, m_s = \pm 1\rangle$ sublevels, but the $|g, m_s = +1\rangle$ and $|g, m_s = -1\rangle$ levels are degenerate in the absence of a magnetic field (as in all experiments reported here). If a strong microwave field at a frequency ν is applied whose energy $h\nu$ matches the energy difference between the $|g, m_s = 0\rangle$ and $|g, m_s = \pm 1\rangle$ levels, then the population of the magnetic sublevels will be equalized. This equalization decreases the population of spins in the $|g, m_s = 0\rangle$ state and consequently reduces the total intensity of fluorescence emitted by the N_V^- center.

Figure 2c shows a swept-frequency ODMR experiment on 100 nm N_V nanodiamond. In this case, an avalanche photodiode (PicoQuant, τ -Spad) was used to collect and detect fluorescence. The gigahertz frequency microwave signal was amplitude-modulated at 200 Hz, and a lock-in amplifier (Signal Recovery 7265) was used to record the synchronized 200 Hz modulation in the detector output as the microwave frequency was swept across the N_V center resonance. Figure 2b shows the output of the lock-in amplifier as a function of microwave frequency. The fluorescence intensity decreased near 2.87 GHz due to the ODMR process. Fitting the observed dip to a Gaussian function yields a 2.868 GHz center frequency and a standard deviation of 18 MHz, shown by the dashed line.

The emission spectra in Figure 2a show that small-diameter nanodiamonds exhibit emission from N_V^0 and Raman scattering in addition to N_V^- emission. To determine how the ODMR contrast varies with wavelength, we used the monochromator and CCD array to measure the emission spectra from ensembles of diamond nanoparticles, with spectra acquired while applying on-resonance (2.87 GHz) and then off-resonance (2.80 GHz) microwave fields. We then determined the effective wavelength-dependent contrast at each wavelength as

$$\text{ODMR contrast}(\lambda) = 100 \times \frac{N_{\text{off-resonance}}(\lambda) - N_{\text{on-resonance}}(\lambda)}{N_{\text{off-resonance}}(\lambda)}$$

Figure 3 shows the effective ODMR contrast for each sample. At short wavelengths the contrast from all samples is reduced

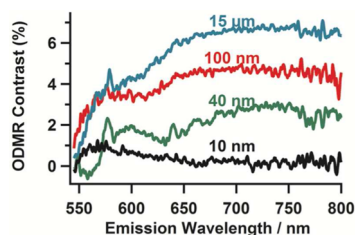


Figure 3. Wavelength-dependent ODMR contrast for nanodiamonds of selected sizes. On-resonance frequency = 2.87 GHz; off-resonance frequency = 2.80 GHz.

because of additional emission from N_V^0 and Raman scattering at these wavelengths. For all samples, the emission reaches a plateau at wavelengths > 650 nm. The existence of this plateau indicates that for emission wavelengths > 650 nm, emission from N_V^- is the only significant emission source. The existence of a size-dependent plateau shows that the decrease in efficiency as a function of size cannot be accounted for by the changes in emission spectrum distribution alone, since at long wavelengths where only N_V^- emits, the contrast remains size-dependent.

Optically Detected Magnetic Resonance Imaging. To demonstrate the ability to use ODMR in an imaging mode to selectively image fluorescence from N_V^- nanodiamond in the presence of nondiamond fluorescent emitters, we characterized samples made by depositing both N_V nanodiamonds and $Al_2O_3:Cr^{3+}$ (ruby) particles onto microscope coverslips, adjusting the amounts deposited to yield similar fluorescence intensities. In tests shown here, we deposited nanodiamond and nanoruby from aqueous suspension into separate regions

separated by a barrier layer made from a silicone polymer. In this way, both fluorescent materials were located within the optical system's field of view at the same time, facilitating quantitative analysis of relevant imaging characteristics. Ruby particles were used in these tests because ruby's fluorescence spectrum, consisting of two sharp peaks near 700 nm with phonon sidebands extending from ~670 to 730 nm (shown in the Supporting Information) is spectrally overlapped with that of nanodiamond and does not bleach, providing a reproducible, spectrally overlapped comparison sample for testing purposes. In these experiments, the detection optics included only a 532 nm notch filter to reject laser scatter; all other emission wavelengths, including emission from N_V^0 nanodiamond, ruby, and Raman scattering, were collected.

Figure 4 shows a series of raw and processed images from 100, 40, and 10 nm nanodiamond. The top two panels in Figure 4 show raw grayscale images of regions containing nanodiamonds and ruby particles obtained with microwaves applied off-resonance (2.93 GHz, Figure 4a,f,k) and on-resonance (2.87 GHz, Figure 4b,g,l) using a conventional grayscale mapping. For each nanodiamond size, the off-resonance and on-resonance images appear nearly identical. However, taking the difference between the images as $I_{2.93\text{ GHz}} - I_{2.87\text{ GHz}}$ yields images (Figure 4c,h,m) that reflect the spatial variations in microwave-induced modulation of the fluorescence intensity, which we refer to as the "ODMR difference image". Since difference values can be positive or negative, these data are represented here as a grayscale image with midgray representing no modulation and white regions, indicating a decrease in intensity upon application of a resonant microwave field. Thus, under these conditions, it is expected that only nanodiamond should exhibit a positive signal, while ruby and other fluorescence chromophores, along with scattered light, should yield signals near zero. To illustrate the signal changes more quantitatively, the fourth row of images (Figure 4d,i,n) shows cross-sectional line cuts through the ODMR difference images along the dashed orange lines. These cross-sectional images show that in the nondiamond regions the signal fluctuates about zero. These fluctuations in intensity are higher in the region containing ruby compared with those in the region containing the hydrophobic barrier layer, demonstrating that non-ODMR fluorescence signals contribute noise to the differential images.

To achieve a more robust signal-to-noise analysis, we note that for photon-counting systems the signal-to-noise ratio is typically limited by shot noise in the number of counts detected. Thus, noise, ΔN_{shot} , scales like the absolute number of counts N as $\Delta N_{\text{shot}} = \sqrt{N}$. Here, $10^4 < N < 10^7$ at all points in each image and the absolute differences between on-resonance and off-resonance images are $\ll N$. Under these conditions noise in each pixel of the difference image will scale approximately as $\Delta N_{\text{shot}} = \sqrt{2N}$, where the 2 arises from the assumption that the noise in the on-resonance and off-resonance images are uncorrelated with each other. Since the modulation in intensity between off-resonance and on-resonance images is small (a few percent), the shot noise at each pixel is approximately $\Delta N_{\text{shot}} = \sqrt{N_{\text{off-resonance}}}$. The signal-to-noise ratio at each pixel for the ODMR experiment can then be predicted to be

$$\frac{\text{ODMR signal}}{\text{noise}} = \frac{N_{2.93\text{ GHz}} - N_{2.87\text{ GHz}}}{\sqrt{2N_{2.93\text{ GHz}}}}$$

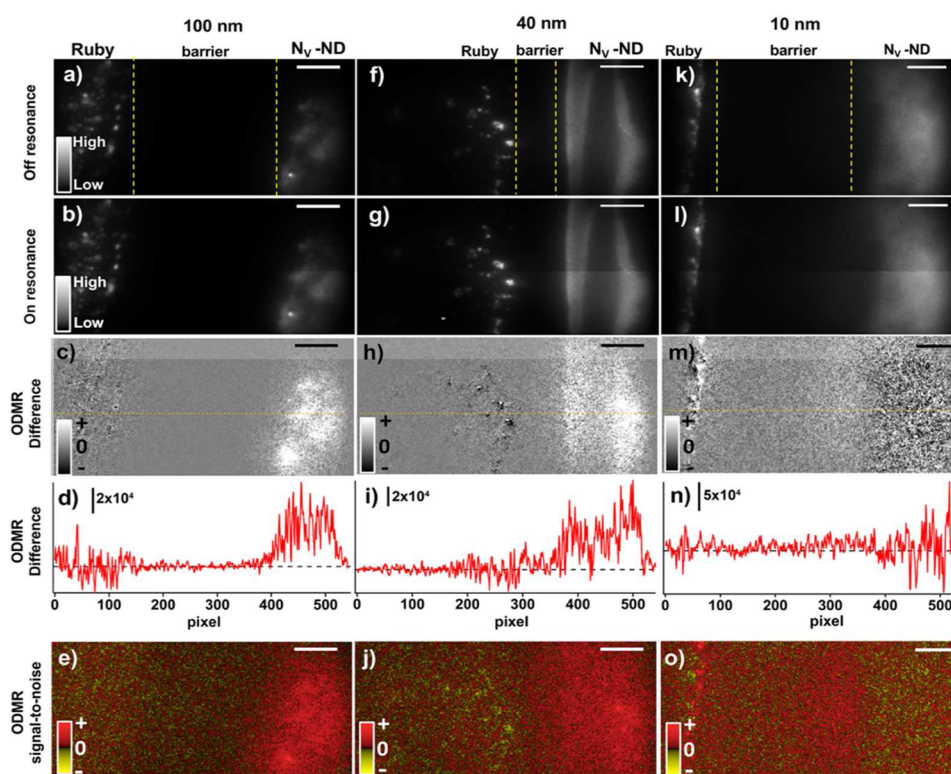


Figure 4. Demonstration of the ability to selectively image nanodiamond using 100 (a–e), 40 (f–j), and 10 nm (k–o) diameter nanodiamond and ruby particles. Images a, f, and k were collected with an off-resonance, 2.93 GHz, microwave frequency. Images b, g, and l were collected with the on-resonance, 2.87 GHz, microwave frequency. Grayscale ranges are nearly identical for panels a, b, f, g, k, and l, ranging from zero to $\sim 6 \times 10^6$ counts per pixel. Images c, h, and m show the difference image $I_{2.93 \text{ GHz}} - I_{2.87 \text{ GHz}}$, representing the microwave-induced modulation in intensity. In this representation nanodiamond should give rise to positive signals, represented as white in the image. Panels d, i, and n show cross-sections through the ODMR difference images. Finally, panels e, j, and o show the ODMR signal-to-noise ratio, as explained in text. Vertical scale ranges are $S/N = (-100, 100)$ for panels e and j and $S/N = (-30, +30)$ for panel o. Horizontal scale bars are $25 \mu\text{m}$ for all images.

This value represents a way to quantitatively assess whether local ODMR difference signals are real or are within the noise limits set by counting statistics at each individual pixel. The fifth row in Figure 4 (Figure 4e,j,o) shows such spatial maps of ODMR signal-to-noise. Here we use a color scale to more clearly show both positive and negative values. For the sample containing 100 nm nanodiamond, the signal-to-noise map (Figure 4e) shows almost uniformly positive signals on the right-hand side of the image where the nanodiamond is located, demonstrating that the ODMR signal is well outside the signal-to-noise limits established by counting statistics. In contrast, in the barrier region and in the region containing ruby particles (left side of image) there are small regions of both positive and negative ODMR signal, but no extended spatial regions where the S/N ratio is large and positive. Similarly, for 40 nm nanodiamond, the ODMR difference image (Figure 4h) shows strong modulation in the region where the nanodiamond is located, and the signal-to-noise map (Figure 4i) shows uniformly high S/N ratio where the nanodiamond is located, but values that fluctuate positively and negatively in the barrier layer and the region where the ruby was located. Finally, for the 10 nm diamond, the ODMR difference signal (Figure 4m) shows only increased noise in the local region, and the S/N map (Figure 4o) shows that there are no extended regions where the signal-to-noise is uniformly positive, suggesting 10 nm particles are unsuitable for imaging. In Figure 4o, a small patch of apparently positive S/N ratio is visible in the region associated with the ruby particles, but further analysis shows

that this feature arises from a small shift in the images due to an electromechanical interaction between the microwave antenna and the microscope stage. Note that Figure 4o is presented on a more sensitive scale compared with those in panels e and j.

An alternative way to assess the ODMR signal is via the percent contrast. This parameter is useful because it is a direct reflection of the nanodiamond and the optical excitation system and should be independent of the properties of the optical collection system. We analyzed the images using one region populated by ruby and one region populated by nanodiamond, and calculated the % contrast as $\% \text{ contrast} = 100 \times \left(\frac{N_{2.93 \text{ GHz}} - N_{2.87 \text{ GHz}}}{N_{2.93 \text{ GHz}}} \right)$, yielding the values shown in Table 1.

For 100 and 40 nm diameter nanodiamond the contrast is several percent, which is readily detectable in imaging mode

Table 1. Imaging-Mode ODMR Percent Contrast Values for Ruby and N_V^- Nanodiamond Regions^a

diameter (nm)	% ODMR contrast		fluorescence lifetime (ns)
	N_V^- ND	ruby	
100	3.37 ± 0.12	0.11 ± 0.09	10.00 ± 0.12
40	2.19 ± 0.11	0.37 ± 0.07	5.38 ± 0.14
10	0.40 ± 0.26	0.04 ± 1.13	≤ 3

^aFluorescence lifetimes for N_V^- nanodiamond samples are also shown with standard deviations of the single-exponential fits being given for each fluorescence lifetime measurement.

using a high-quality array detector with sufficiently low dark counts. The 10 nm diamond contrast is less than 1%, challenging the signal-to-noise capabilities of the optical detection. As expected, the regions with background from ruby show apparent ODMR contrast values that are very close to zero.

Fluorescence Lifetimes of N_V Centers. The above data indicate that, under equivalent imaging conditions, the fractional modulation in intensity associated with application of a microwave field (the “ODMR contrast”) is poorer with the smallest diameter (10 nm) nanodiamond compared with larger (40 and 100 nm) nanodiamond. To better understand the origin of these observations, we measured the fluorescence lifetime of the nanodiamond samples using a tunable pulsed laser (~ 3 ns pulse width) and a fast (2 GHz) photodiode. Figure 5 shows representative fluorescence decay curves from

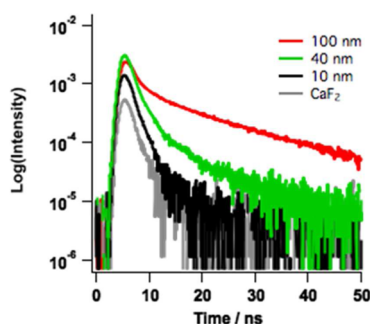


Figure 5. Fluorescence lifetime measurements from N_V nanodiamonds of different diameters and the reflection of the excitation laser off of the CaF_2 window to show the instrument response function. Vertical axis in arbitrary units.

nanodiamond samples of different diameters. Fluorescence lifetimes from samples of different sizes were fit to single exponents over the 12–34 ns time interval. As shown in Table 1, the fluorescence lifetime decreases from 10.00 ± 0.12 to 5.38 ± 0.14 ns as the nanodiamond size decreases from 100 to 40 nm. The lifetime of the 10 nm nanodiamond could not be measured as it is indistinguishable from the apparent lifetime of nonfluorescence background signals arising from scattering off the underlying CaF_2 substrate; this indicates the lifetime is shorter than the 3 ns excitation laser pulse. Thus, these data show that the small-diameter nanoparticles have higher rates of fluorescence decay compared to larger diameter nanoparticles.

These lifetime studies suggest that the reduction in contrast for small-diameter nanodiamonds is likely associated with the presence of additional nonradiative decay pathways that are not spin-selective. Such processes would have the effect of reducing the effectiveness of the spin-pumping and thereby decrease the ODMR contrast. To test whether the contrast could be enhanced for small-diameter nanodiamond by increasing laser power, we conducted a laser power ODMR study. Those experiments (results presented in SI) revealed that the contrast is not significantly enhanced using higher incident laser power. In addition, we observed that higher incident laser powers induce spectral broadening and flatten the zero phonon line of N_V^- . These results, in agreement with prior reports by others,³¹ indicate that the loss in contrast for small-diameter nanodiamond cannot be easily rectified by using different conditions of the optical or microwave excitation.

DISCUSSION

Our data show that it is possible to selectively image N_V nanodiamond in the presence of other emitters by using ODMR in an imaging mode by direct subtraction of off-resonance and on-resonance images. The ability to selectively image one type of nanoparticle in the presence of other fluorescent moieties has significant potential for use of N_V nanodiamond as an analytical probe in chemistry and biology. For example, one of the key challenges in understanding the fate, transport, and uptake of nanomaterials in the environment is the difficulty of distinguishing nanoparticle fluorescence from spectrally overlapped signals such as Raman scattering and fluorescence from other species. While our experiments demonstrate that direct ODMR imaging is possible, the ability to achieve this selective imaging decreases significantly as the particle size decreases <40 nm due to reduction in ODMR contrast. This reduction is due to changes in the emission spectrum and a decrease in the lifetime of the N_V centers. These changes reduce the ODMR contrast from a maximum theoretical value of $\sim 30\%$ reported using high-quality macroscopic diamond samples,⁵⁶ to lower values of 5% or less for nanodiamonds. While ODMR is in principle a “background-free” imaging technique, to effectively use N_V nanodiamonds in detection systems, it is important to address the critical signal-to-noise issues that control the ability to selectively identify N_V nanodiamond from within more complex systems. We consider first the intrinsic S/N properties of the detection system.

The ability to selectively detect ODMR relies on the ability to subtract adjacent images with S/N ratio sufficiently high to distinguish ODMR contrast from noise. In Figure 4, background signals other than ODMR are close to zero but the associated shot noise gives rise to pixel-by-pixel fluctuations. Under the conditions of our experiment (20 \times magnification, 0.5 numerical aperture objective, $f/3.7$ monochromator, and 13 μm CCD element size), the diffraction-limited Airy disk on the CCD produced by a point source is 6 μm diameter, and light emitted from any object of <1.5 μm diameter is focused onto a single pixel. Detection of *individual*, isolated nanodiamonds would require sufficient ODMR contrast on individual CCD pixels to exceed the shot noise arising from the background fluorescence, while more spatially extended ensembles of nanodiamonds (as in our experiments, Figure 4a–j) can be easily identified by a high S/N ratio that is distributed across many pixels.

The second factor controlling the ability to use ODMR imaging is the size-dependent changes in the nanodiamond spectrum and dynamics. There are two primary contributors to these changes: (1) shifting of the charge state from N_V^- to N_V^0 at small sizes and (2) introduction of new relaxation pathways. These phenomena are both associated with the diamond surfaces. Prior studies have shown that changes in the electrostatic potential at nanodiamond surfaces induce a shift in the charge state of the N_V^- center to favor the neutral N_V^0 center.^{46–48} This shift is evidenced in Figure 2a as increased emission near 630 nm for nanodiamonds that are ~ 40 nm and below in diameter. While this change in charge state decreases the ODMR contrast when emission is integrated over all wavelengths (as in Table 1), it should not affect the contrast at long wavelengths (e.g., 700–800 nm) where the only emission is from N_V^- . However, Figure 3 shows that the ODMR contrast is reduced even at long wavelengths, implying that other size-dependent factors also are important. The ability to achieve

ODMR contrast is strongly dependent on the relative rates of fluorescence and spin-dependent intersystem crossing. Figure 5 shows that as the nanoparticle size decreases below 100 nm, the lifetime decreases, becoming <3 ns for 10 nm nanodiamond. As a consequence, the overall quantum efficiency for luminescence decreases and other optical processes such as Raman scattering become more apparent when emission spectra are normalized to similar intensities. Thus, the appearance of Raman peaks at 500–600 nm for nanoparticles < 40 nm diameter is due in part to the reduced intensity from N_V^- emission.

The size-dependent changes in spectral distribution and radiative lifetime both highlight the important role of the nanoparticle surfaces and surface defects that facilitate non-radiative relaxations. If the rates of these nonradiative processes are comparable to or greater than that of relaxation through the single-spin system, then the effectiveness of the spin-pumping is reduced, leading to reduced ODMR contrast. Attempts to compensate for the reduced pumping efficiency by increasing the incident laser fluence resulted in broadening of the lines and did not significantly increase the contrast, likely due to heating effects.

These results provide a guide for understanding the optimum choice of N_V nanodiamond for different types of imaging and sensing applications. Our results using nanodiamonds with oxidized surfaces suggest that 40 nm diameter provides a balance between ODMR contrast and N_V^- emission. It is possible that further improvements might be achievable by using nanoparticles with different surface terminations to maintain more N_V centers in the negative charge state (N_V^-) and by applying surface treatments that reduce the number of midgap defect states. Ultimately the enhanced understanding of size-dependent N_V^- dynamics obtained in these studies will be important in the future development of even more advanced imaging techniques that seek to use the N_V^- center's long coherence time and other quantum-based properties to achieve new imaging modalities.^{34–41,54}

CONCLUSIONS

By modulating the frequency of an applied microwave field, optically detected magnetic resonance induces selective modulation of the intensity of fluorescence emission from N_V^- nanodiamond. We have shown that by using differential imaging methods in which images are acquired with the microwave field on-resonance and off-resonance and then subtracted, the N_V nanodiamond can be selectively imaged in the presence of other fluorophores. The use of very small N_V nanodiamond for imaging applications is limited by surface states that alter the nanodiamond charge state and reduce the efficiency of optical spin-pumping. As the ODMR contrast decreases to below ~2%, effective use of ODMR to selectively identify N_V nanodiamond in complex matrices may require more elaborate differencing techniques than the direct subtraction method applied here and/or improved control over the nanodiamond surfaces to reduce the effects of surface states. However, for nanodiamonds with diameters as small as 40 nm, an ODMR contrast of several percent is well outside the noise limits of most modern imaging systems and will enable new selective imaging modalities based on the charge and spin properties of N_V centers.

ASSOCIATED CONTENT

Supporting Information

The Supporting Information is available free of charge on the ACS Publications website at DOI: 10.1021/acs.analchem.7b03157.

Emission spectra of detonation nanodiamond and monocrystalline diamond, emission spectra of 100 nm N_V nanodiamond using various excitation laser powers, ODMR response of 100 nm N_V nanodiamond at 100 mW and 500 mW excitation laser powers, and TEM images and DLS characterization of nanodiamond samples (PDF)

AUTHOR INFORMATION

Corresponding Author

*E-mail: rjhamers@wisc.edu. Tel. (work): 608-262-6371. Fax: 608-262-0453.

ORCID

Joseph T. Buchman: 0000-0001-5827-8513

Christy L. Haynes: 0000-0002-5420-5867

Randall H. Goldsmith: 0000-0001-9083-8592

Robert J. Hamers: 0000-0003-3821-9625

Notes

The authors declare the following competing financial interest(s): O.A.S. is President of Adámas Nanotechnologies.

ACKNOWLEDGMENTS

This work was supported by the National Science Foundation (NSF) via the Centers for Chemical Innovation Program Award CHE-1503408, the Center for Sustainable Nanotechnology. J.T.B. was supported by the University of Minnesota Biotechnology Training Grant Program through the National Institutes of Health. Fabrication of microwave antennas was supported by Office of Naval Research Grant No. N00014-13-1-0226 to Z.M. TEM work in this study was carried out in the Characterization Facility, University of Minnesota, which receives partial support from NSF through the MRSEC program. R.H.G. and J.N. acknowledge support from the National Science Foundation via Grant No. CHE-1254936 for initial studies of N_V resonance phenomena. N_V nanodiamond samples were produced by Adámas Nanotechnologies using support from the National Heart, Lung, and Blood Institute, National Institutes of Health (NIHLBI), under Contract No. HHSN268201500010. We acknowledge F. J. Heremans and D. D. Awschalom for helpful conversations, C. N. Nunn of Adámas for help with sample preparation, and A. Shames of Ben-Gurion University of Negev for providing EPR data on N_V center content in the samples.

REFERENCES

- (1) Szakal, C.; Ugelow, M. S.; Gorham, J. M.; Konicek, A. R.; Holbrook, R. D. *Anal. Chem.* **2014**, *86*, 3517–3524.
- (2) Hayden, O.; Payne, C. K. *Angew. Chem., Int. Ed.* **2005**, *44*, 1395–1398.
- (3) Huynh, K. A.; Siska, E.; Heithmar, E.; Tadjiki, S.; Pergantis, S. A. *Anal. Chem.* **2016**, *88*, 4909–4916.
- (4) Ermolin, M. S.; Fedotov, P. S. *Rev. Anal. Chem.* **2016**, *35*, 185–199.
- (5) Benn, T. M.; Westerhoff, P. *Environ. Sci. Technol.* **2008**, *42*, 4133–4139.
- (6) Marbella, L. E.; Millstone, J. E. *Chem. Mater.* **2015**, *27*, 2721–2739.

- (7) Cooke, P. M. *Anal. Chem.* **2000**, *72*, 169–188.
- (8) Huang, B.; Wang, W. Q.; Bates, M.; Zhuang, X. W. *Science* **2008**, *319*, 810–813.
- (9) von Diezmann, A.; Shechtman, Y.; Moerner, W. E. *Chem. Rev.* **2017**, *117*, 7244–7275.
- (10) Tan, Y. Z.; Jin, S.; Hamers, R. J. *ACS Appl. Mater. Interfaces* **2013**, *5*, 12975–12983.
- (11) Tvrđy, K.; Kamat, P. V. *J. Phys. Chem. A* **2009**, *113*, 3765–3772.
- (12) van Sark, W. G. J. H.; Frederix, P. L. T. M.; Van den Heuvel, D. J.; Gerritsen, H. C.; Bol, A. A.; van Lingen, J. N. J.; de Mello Donega, C.; Meijerink, A. *J. Phys. Chem. B* **2001**, *105*, 8281–8284.
- (13) Klyachkovskaya, E. V.; Vashchenko, S. V.; Stupak, A. P.; Gaponenko, S. V. *J. Appl. Spectrosc.* **2010**, *77*, 732–736.
- (14) Saurabh, S.; Perez, A. M.; Comerci, C. J.; Shapiro, L.; Moerner, W. E. *J. Am. Chem. Soc.* **2016**, *138*, 10398–10401.
- (15) Kolmakov, K.; Wurm, C. A.; Meineke, D. N. H.; Gottfert, F.; Boyarskiy, V. P.; Belov, V. N.; Hell, S. W. *Chem. - Eur. J.* **2014**, *20*, 146–157.
- (16) Resch-Genger, U.; Grabolle, M.; Cavaliere-Jaricot, S.; Nitschke, R.; Nann, T. *Nat. Methods* **2008**, *5*, 763–775.
- (17) Bu, X. B.; Chen, H. P.; Gai, H. W.; Yang, R. H.; Yeung, E. S. *Anal. Chem.* **2009**, *81*, 7507–7509.
- (18) He, H.; Xie, C.; Ren, J. *Anal. Chem.* **2008**, *80*, 5951–5957.
- (19) Bandyopadhyay, S.; Peralta-Videa, J. R.; Gardea-Torresdey, J. L. *Environ. Eng. Sci.* **2013**, *30*, 118–125.
- (20) Hsiao, W. W. W.; Hui, Y. Y.; Tsai, P. C.; Chang, H. C. *Acc. Chem. Res.* **2016**, *49*, 400–407.
- (21) Wu, Y. Z.; Jelezko, F.; Plenio, M. B.; Weil, T. *Angew. Chem., Int. Ed.* **2016**, *55*, 6586–6598.
- (22) Reineck, P.; Francis, A.; Orth, A.; Lau, D. W. M.; Nixon-Luke, R. D. V.; Rastogi, I. D.; Razali, W. A. W.; Cordina, N. M.; Parker, L. M.; Sreenivasan, V. K. A.; Brown, L. J.; Gibson, B. C. *Adv. Opt. Mater.* **2016**, *4*, 1549–1557.
- (23) Pansare, V. J.; Hejazi, S.; Faenza, W. J.; Prud'homme, R. K. *Chem. Mater.* **2012**, *24*, 812–827.
- (24) Davies, G.; Hamer, M. F. *Proc. R. Soc. London, Ser. A* **1976**, *348*, 285–298.
- (25) Wang, X. Y.; Landis, E. C.; Franking, R.; Hamers, R. J. *Acc. Chem. Res.* **2010**, *43*, 1205–1215.
- (26) Krueger, A.; Lang, D. *Adv. Funct. Mater.* **2012**, *22*, 890–906.
- (27) Stavis, C.; Clare, T. L.; Butler, J. E.; Radadia, A. D.; Carr, R.; Zeng, H. J.; King, W. P.; Carlisle, J. A.; Aksimentiev, A.; Bashir, R.; Hamers, R. J. *Proc. Natl. Acad. Sci. U. S. A.* **2011**, *108*, 983–988.
- (28) Chapman, R.; Plakhoitnik, T. *Opt. Lett.* **2013**, *38*, 1847–1849.
- (29) Igarashi, R.; Yoshinari, Y.; Yokota, H.; Sugi, T.; Sugihara, F.; Ikeda, K.; Sumiya, H.; Tsuji, S.; Mori, I.; Tochio, H.; Harada, Y.; Shirakawa, M. *Nano Lett.* **2012**, *12*, 5726–5732.
- (30) Gruber, A. *Science* **1997**, *276*, 2012–2014.
- (31) Singam, S. K. R.; Motylewski, J.; Monaco, A.; Gjorgievska, E.; Bourgeois, E.; Nesládek, M.; Giugliano, M.; Goovaerts, E. *Phys. Rev. Appl.* **2016**, *6*, 064013.
- (32) Hegyi, A.; Yablonovitch, E. *Nano Lett.* **2013**, *13*, 1173–1178.
- (33) Sarkar, S. K.; Bumb, A.; Wu, X. F.; Sochacki, K. A.; Kellman, P.; Brechbiel, M. W.; Neuman, K. C. *Biomed. Opt. Express* **2014**, *5*, 1190–1202.
- (34) Balasubramanian, G.; Chan, I. Y.; Kolesov, R.; Al-Hmoud, M.; Tisler, J.; Shin, C.; Kim, C.; Wojcik, A.; Hemmer, P. R.; Krueger, A.; Hanke, T.; Leitenstorfer, A.; Bratschitsch, R.; Jelezko, F.; Wrachtrup, J. *Nature* **2008**, *455*, 648–651.
- (35) Taylor, J. M.; Cappellaro, P.; Childress, L.; Jiang, L.; Budker, D.; Hemmer, P. R.; Yacoby, A.; Walsworth, R.; Lukin, M. D. *Nat. Phys.* **2008**, *4*, 810–816.
- (36) Maze, J. R.; Stanwix, P. L.; Hodges, J. S.; Hong, S.; Taylor, J. M.; Cappellaro, P.; Jiang, L.; Dutt, M. V. G.; Togan, E.; Zibrov, A. S.; Yacoby, A.; Walsworth, R. L.; Lukin, M. D. *Nature* **2008**, *455*, 644–647.
- (37) McGuinness, L. P.; Yan, Y.; Stacey, A.; Simpson, D. A.; Hall, L. T.; Maclaurin, D.; Praver, S.; Mulvaney, P.; Wrachtrup, J.; Caruso, F.; Scholten, R. E.; Hollenberg, L. C. L. *Nat. Nanotechnol.* **2011**, *6*, 358–363.
- (38) Hall, L. T.; Cole, J. H.; Hill, C. D.; Hollenberg, L. C. L. *Phys. Rev. Lett.* **2009**, *103*, 220802.
- (39) Dolde, F.; Fedder, H.; Doherty, M. W.; Nobauer, T.; Rempp, F.; Balasubramanian, G.; Wolf, T.; Reinhard, F.; Hollenberg, L. C. L.; Jelezko, F.; Wrachtrup, J. *Nat. Phys.* **2011**, *7*, 459–463.
- (40) Grotz, B.; Beck, J.; Neumann, P.; Naydenov, B.; Reuter, R.; Reinhard, F.; Jelezko, F.; Wrachtrup, J.; Schweinfurth, D.; Sarkar, B.; Hemmer, P. *New J. Phys.* **2011**, *13*, 055004.
- (41) Toyli, D. M.; de las Casas, C. F.; Christle, D. J.; Dobrovitski, V. V.; Awschalom, D. D. *Proc. Natl. Acad. Sci. U. S. A.* **2013**, *110*, 8417–8421.
- (42) Levchenko, A. O.; Vasil'ev, V. V.; Zibrov, S. A.; Zibrov, A. S.; Sivak, A. V.; Fedotov, I. V. *Appl. Phys. Lett.* **2015**, *106*, 102402.
- (43) Kaviani, M.; Deák, P.; Aradi, B.; Frauenheim, T.; Chou, J.-P.; Gali, A. *Nano Lett.* **2014**, *14*, 4772–4777.
- (44) Cui, S.; Hu, E. L. *Appl. Phys. Lett.* **2013**, *103*, 051603.
- (45) Hauf, M. V.; Grotz, B.; Naydenov, B.; Dankerl, M.; Pezzagna, S.; Meijer, J.; Jelezko, F.; Wrachtrup, J.; Stutzmann, M.; Reinhard, F.; Garrido, J. A. *Phys. Rev. B: Condens. Matter Mater. Phys.* **2011**, *83*, 081304.
- (46) Maier, F.; Riedel, M.; Mantel, B.; Ristein, J.; Ley, L. *Phys. Rev. Lett.* **2000**, *85*, 3472–3475.
- (47) Grotz, B.; Hauf, M. V.; Dankerl, M.; Naydenov, B.; Pezzagna, S.; Meijer, J.; Jelezko, F.; Wrachtrup, J.; Stutzmann, M.; Reinhard, F.; Garrido, J. A. *Nat. Commun.* **2012**, *3*, 729.
- (48) Ohashi, K.; Roskopf, T.; Watanabe, H.; Loretz, M.; Tao, Y.; Hauert, R.; Tomizawa, S.; Ishikawa, T.; Ishi-Hayase, J.; Shikata, S.; Degen, C. L.; Itoh, K. M. *Nano Lett.* **2013**, *13*, 4733–4738.
- (49) Zvyagin, A. V.; Manson, N. B. In *Ultranacocrystalline Diamond*, 2nd ed.; Shenderova, O. A., Gruen, D. M., Eds.; Elsevier: New York, 2012; pp 327–354, DOI: [10.1016/B978-1-4377-3465-2.00010-4](https://doi.org/10.1016/B978-1-4377-3465-2.00010-4).
- (50) Santori, C.; Barclay, P. E.; Fu, K.-M. C.; Beausoleil, R. G. *Phys. Rev. B: Condens. Matter Mater. Phys.* **2009**, *79*, 125313.
- (51) Chung, P. H.; Perevedentseva, E.; Cheng, C. L. *Surf. Sci.* **2007**, *601*, 3866–3870.
- (52) Shames, A. I.; Osipov, V. Y.; Boudou, J. P.; Panich, A. M.; von Bardeleben, H. J.; Treussart, F.; Vul' A. Y. *J. Phys. D: Appl. Phys.* **2015**, *48*, 155302.
- (53) Shenderova, O.; Nunn, N.; Oeckinghaus, T.; Torelli, M.; McGuire, G.; Smith, K.; Danilov, E.; Reuter, R.; Wrachtrup, J.; Shames, A.; Filonova, D.; Kinev, A. *Proc. SPIE* **2017**, *1011803*, 1011803-1.
- (54) Horowitz, V. R.; Aleman, B. J.; Christle, D. J.; Cleland, A. N.; Awschalom, D. D. *Proc. Natl. Acad. Sci. U. S. A.* **2012**, *109*, 13493–13497.
- (55) Robledo, L.; Bernien, H.; Sar, T. v. d.; Hanson, R. *New J. Phys.* **2011**, *13*, 025013.
- (56) Popa, J.; Gaebel, T.; Neumann, P.; Jelezko, F.; Wrachtrup, J. *Isr. J. Chem.* **2006**, *46*, 393–398.

Supporting Information for

Optically detected magnetic resonance for selective imaging of diamond nanoparticles

Margaret E. Robinson[†], James D. Ng[†], Huilong Zhang[‡], Joseph T. Buchman[§], Olga A. Shenderova,[#] Christy L. Haynes[§], Zhenqiang Ma[‡], Randall H. Goldsmith[†], and Robert J. Hamers^{†*}

[†]Department of Chemistry, University of Wisconsin-Madison, 1101 University Avenue, Madison, WI 53706, United States

[#]Adámas Nanotechnologies, 8100 Brownleigh Dr, Raleigh, NC 27617

[‡]Department of Electrical and Computer Engineering, University of Wisconsin-Madison, 3445 Engineering Hall, 1415 Engineering Drive, Madison, Wisconsin 53706

[§]Department of Chemistry, University of Minnesota, 207 Pleasant St SE, Minneapolis, MN 55455, United States

*Email: rjhamers@wisc.edu Phone (work): 608-262-6371, Fax: 608-262-0453

Materials and chemicals

Detonation nanodiamond (4-5 nm) were purchased from Nanoscale and Amorphous Materials, Inc). Monocrystalline nanodiamond (MS Y 0-0.03 micron) were obtained from Microdiamant. Adámas Nanotechnologies (Raleigh, NC) provided suspensions of oxidized, size-selected (0.1% by weight) with enhanced concentrations of N_V^- centers with nominal diameters ranging from 10 to 100 nm. Transmission electron microscopy analysis was performed by taking nanodiamond stock suspensions and bath sonicating (Branson M1800, 40KHz) for 2 minutes. The stocks were diluted in methanol and sonicated briefly to ensure they were well dispersed. Then, a 2 μ L aliquot of the suspension was dropped onto a 200 mesh copper grid with Formvar and carbon supports from Ted Pella, Inc. (Redding, CA). The grid was air-dried near an open 65 °C oven for 5 minutes. An FEI Tecnai T12 transmission electron microscope was used at 120 kV to acquire images of the nanodiamonds. Images were manually analyzed for particle area using ImageJ on $N=200$ particles for each nanodiamond sample.

S1. Determination of N_V^- concentration by ESR: Continuous wave X-band (frequency 9.4 GHz) EPR measurements on polycrystalline samples were carried out using a Bruker EMX - 220 spectrometer at room temperature. Precise determination of g-factors (for $S = 1/2$ centers) and densities of the corresponding paramagnetic centers (N_s) were done by comparison with a reference sample - well purified detonation nanodiamond powder with $g = 2.0028(2)$ and $N_s = 6.3 \times 10^{19}$ spins/g.¹ The integral intensity of the so-called “characteristic $g = 4.26$ line” is proportional to the content of N_V^- centers measured by double integration of the entire polycrystalline triplet pattern.² This allows for quantification of N_V^- triplet centers by comparison of the integral intensity of $g = 4.26$ line in the fluorescent microdiamond sample

with the known NV- content (5.4×10^{17} spin/g) with the intensities of the corresponding lines in the EPR spectra of samples under study.³

S2. Emission spectra from non-irradiated nanodiamond

Emission spectra of detonation nanodiamond and monocrystalline nanodiamond were collected using the same optics described in Figure 1a. We note the absence of a peak at 585 nm, suggesting that the 585 nm peak in Figure 1b arises as a consequence of the irradiation process used to enhance the N_V concentration.

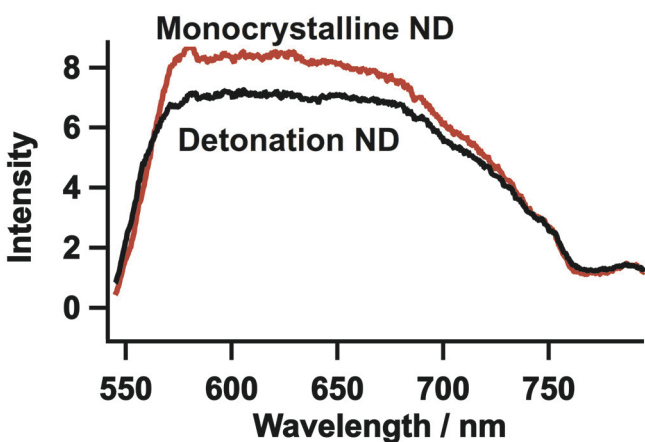


Figure S1: Emission spectra of detonation nanodiamond and monocrystalline nanodiamond collected with 532 nm, 100 mW excitation laser power.

S3. Laser power study

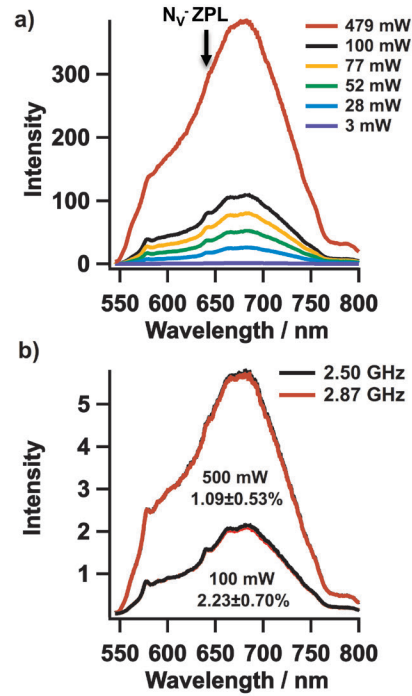


Figure S3: a) Photoluminescence spectra of 100 nm nanodiamond dried onto a glass coverslip collected using various 532 nm excitation laser powers. The broadened zero phonon line of N_V^- is indicated with an arrow b) Optically detected magnetic resonance on the same sample using 100 and 500 mW laser powers. The % ODMR contrasts, $1.09 \pm 0.53\%$ and $2.23 \pm 0.70\%$ for 500 and 100 mW lasers powers, respectively, are not significantly different.

Photoluminescence spectra of 100 nm N_V^- nanodiamond were collected at various 532 nm excitation laser powers in order to determine the ideal excitation power for future optically detected magnetic resonance (ODMR) experiments. We observed that at very high excitation power, ~ 500 mW, that the zero phonon line (ZPL) of N_V^- is broadened and flattened into the larger phonon side band. ODMR was performed on the same sample using 100 mW and 500 mW laser powers. Percent ODMR contrast was calculated using Equation (1) and determined to be $1.09 \pm 0.53\%$ and $2.23 \pm 0.70\%$ for 500 and 100 mW lasers powers, respectively. These %contrasts are not statistically significantly different. For this reason we chose to use a 100 mW laser power for future studies.

S4. Characterization of nanodiamond particle size

Each nanodiamond sample was characterized by dynamic light scattering (Malvern Zetasizer Nano ZS) and by transmission electron microscopy (Figure S3) to assess particle size and distribution. Results are summarized in Table S3.

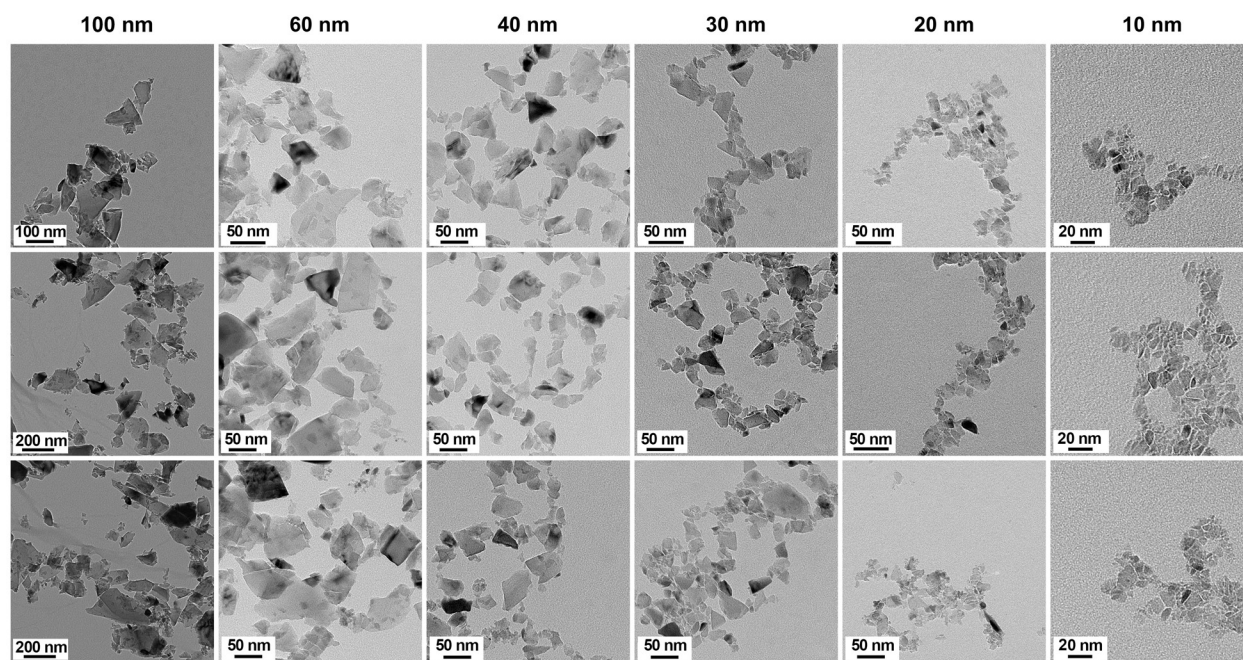


Figure S3: Representative transmission electron microscope images of nanodiamond (Adámas Nanotechnologies) with nominal nanodiamond diameters listed above each column.

Table S1: Nanodiamond particle size analysis was accomplished by dynamic light scattering and transmission electron microscopy.

Adámas Nanotechnologies reported diameter	Dynamic light scattering		Transmission electron microscopy
	Polydispersity index	Number Mean (nm)	Mean Diameter (nm)
100 nm	0.1	116.4 ± 4.9	55.9
60 nm	0.1	58.5 ± 2.5	35.1
40 nm	0.1	46.3 ± 4.2	39.1
30 nm	0.2	30.4 ± 1.4	24.3
20 nm	0.3	20.6 ± 4.0	12.7
10 nm	0.2	35.4 ± 4.7	9.4

S5. Synthesis of nanoruby and emission spectra.

Ruby particles were synthesized following the approach of Rani, et al.⁴ by mixing aqueous solutions of aluminum nitrate ($\text{Al}(\text{NO}_3)_3$), urea ($\text{CO}(\text{NH}_2)_2$), and chromium(III) nitrate ($\text{Cr}(\text{NO}_3)_3$ in mole ratios of Al: urea: Cr= 1.0 : 2.49 : 0.01 and placing the solution in a 500 °C box furnace for 15 minutes, yielding $\text{Al}_{2-x}\text{Cr}_x\text{O}_3$ with $x \sim 0.01$) The pink product was crushed in a mortar and pestle before use in experiments.

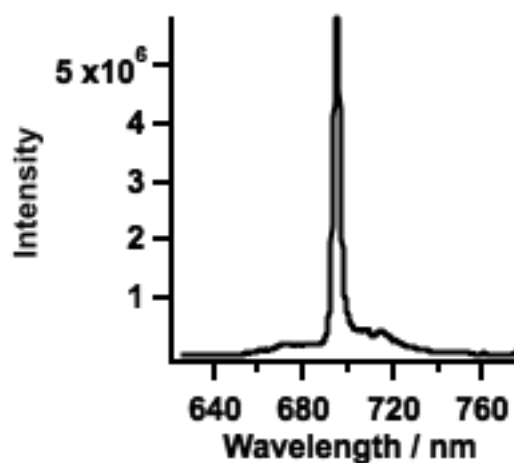


Figure S4: Emission spectrum of the synthesized ruby particles collected using the optical apparatus shown in Fig1 of the main paper.

References:

1. Osipov, V. Y.; Shames, A. I.; Enoki, T.; Takai, K.; Baidakova, M. V.; Vul, A. Y., Paramagnetic defects and exchange coupled spins in pristine ultrananocrystalline diamonds. *Diamond Relat. Mater.* **2007**, *16*, 2035-2038.
2. Shames, A. I.; Osipov, V. Y.; Boudou, J. P.; Panich, A. M.; von Bardeleben, H. J.; Treussart, F.; Vul', A. Y., Magnetic resonance tracking of fluorescent nanodiamond fabrication. *J. Phys.D. Appl. Phys.* **2015**, *48*, 155302.

3. Shenderova, O.; Nunna, N.; Oeckinghaus, T.; Torellia, M.; McGuire, G.; Smith, K.; Danilov, E.; Reuter, R.; Wrachtrup, J.; Shames, A. In *Commercial quantities of ultrasmall fluorescent nanodiamonds containing color centers*, Proc. of SPIE Vol, 2017; pp 1011803-1.
4. Rani, G.; Sahare, P. D., Structural and photoluminescent properties of Al₂O₃: Cr³⁺ nanoparticles via solution combustion synthesis method. *Adv. Powder Technol.* **2014**, *25*, 767-772.